Ground observations to characterize the spatial gradients and vertical structure of orographic precipitation – Experiments in the inner region of the Great Smoky Mountains

Olivier P. Prat [*], Ana P. Barros

Civil and Environmental Engineering Department, Pratt School of Engineering, Duke University, Durham, North Carolina, United States

S U M M A R Y

A new rain gauge network was installed in the Great Smoky Mountains National Park (GSMNP) in the Southern Appalachians since 2007 to investigate the space–time distribution of precipitation in the inner mountain region. Exploratory Intense Observing Periods (IOPs) have been conducted in the summer and fall seasons to devise optimal long-term monitoring strategies, and Micro Rain Radars (MRR) were deployed twice in July/August and October/November 2008 at a mountain ridge location and a nearby valley. Rain gauge and MRR observations were analyzed to characterize seasonal (summer/fall) and orographic (valley/ridge) precipitation features. The data show that summer precipitation is characterized by large event-to-event variability including both stratiform and convective properties. During fall, stratiform precipitation dominates and rainfall is two times more frequent at the ridge than in the valley, corresponding to a 100% increase in cumulative rainfall at high elevation. For concurrent rain events, the orographic enhancement effect is on the order of 60%. Evidence of a seasonal signature in the drop size distribution (DSD) was found with significantly heavier tails (larger raindrops) for summer DSDs at higher elevations, whereas no significant differences were observed between ridge and valley locations during fall deployment. However, physically-based modeling experiments suggest that there are inconsistencies between the reflectivity profiles and MRR DSD estimates when large raindrop sizes are present. The number of very small drops is very high (up to two orders of magnitude) at high elevations as compared to the typical values in the literature, which cannot be explained only by fog and drizzle and suggest an important role for mixed phase processes in determining the shape of the DSD below the brightband. Because numerical modeling experiments show that coalescence is the dominant microphysical mechanism for DSD evolution for the relatively low to moderate observed rain rates characteristic of mountainous regions, it is therefore critical to clarify the shape and parameters that characterize the lefthand side of the DSD in mountainous regions. Finally, whereas low cost Micro Rain Radars (MRR) were found particularly useful for qualitative description of precipitation events and to identify rain/snow melting conditions, when compared against collocated rain gauges, MRR Quantitative Precipitation Estimation (QPE) is not reliable. Place-based calibration and reliance upon physically-based QPE retrieval algorithms can improve their utility.

1. Introduction

The conventional conceptual model of orographic precipitation contrasting upwind enhancement vs. (downwind) rainshadow effects describes well mountain-scale spatial gradients of precipitation, but it is inadequate to explain the space–time distribution of precipitation in the inner regions of complex mountain systems. For example, Barros and Lettenmaier (1993, 1994), Barros et al. (2000) and Lang and Barros (2002) among others documented very large along-mountain and ridge-valley gradients of up to 1000 mm/10 km. These regions cannot be observed using standard weather radars because of ground-clutter effects, and capturing the space–time variability of precipitation across mountainous regions remains a major challenge for satellite-based precipitation estimates (e.g. Barros and Tao, 2008). To address this challenge, a new observational network has been installed in the Great Smoky Mountains National Park (GSNP) in the Southern Appalachians, and exploratory Intense Observing Periods (IOPs) have been conducted to devise optimal long-term monitoring strategies. Rainfall varies greatly across the mountains of North Carolina causing widespread flooding and landslides (Wooten et al., 2008). For instance rainfall

* Corresponding author. Address: Duke University, Box 90287, 2457 CIEMAS Fitzpatrick Bldg., Durham, NC 27708, United States. Tel.: +1 919 660 5487; fax: +1 919 660 5219.
  E-mail address: oprat@duke.edu (O.P. Prat).

accumulations of up to 470 mm were measured over a 24 h period during the passage of Hurricanes Frances and Ivan respectively in 2004 in Western North Carolina (by then tropical depressions). Rainfall records from (mostly low-lying) rain gauges indicated orographic enhancement factors on the order of 300% around Ashville, NC. In that sense, the region offers a unique setting to study both warm and cold season orographic precipitation regimes: (a) a cold season orographic precipitation regime associated with post-frontal northwest flows that leads to a west (high)–east (low) gradient of snowfall; and (b) a warm season orographic precipitation regime associated with the passage of intense storm systems including southerly and easterly tropical depressions. During the wintertime, there is also evidence of isolated convective activity (Barros and Kuligowski, 1998). How the terrain modifies the microphysical and dynamical processes that govern precipitation as weather systems approach and pass over the mountains is not yet understood, and the effect of the terrain on localized convective storms is also partially unknown (Smith, 1979; Barros and Lettenmaier, 1994; Roe, 2005 among others). While numerous studies were conducted for high mountainous regions such as the Cascades, the Alps or the Himalayas among others (Barros and Lettenmaier, 1994; Smith et al., 2003, 2005; Lang and Barros, 2004), little research is available for the region of the Southern Appalachian Mountains, characterized by complex relief but moderate altitudes (maximum peak elevation around 2000 m; Barros and Kuligowski, 1998; Perry and Konrad, 2006).

A high-spatial resolution rain gauge network has been installed in the region since summer 2007. Two exploratory field campaigns were conducted in the Great Smoky Mountains National Park (GSMNP) in July–August 2008 and in October–November 2008 involving the deployment of vertically pointing radars in order to investigate the mechanisms and microphysical properties of warm/cold and mountain/valley precipitation. The objective was to collect observations to document summertime/fall interactions between landform and storm systems in the Great Smoky Mountains with an eye at devising an optimal long-term monitoring plan that can focus on key physical processes. Those microphysical observations were integrated into a dense rain gauge network designed specifically to capture orographic precipitation gradients between inner valleys and surrounding ridges.

Here, we present an analysis of the observations collected during the intense observation periods (IOPs) with emphasis on characterizing the diurnal cycle of rainfall and the contrast between summer and fall precipitation in the Great Smoky Mountains, as well as spatial variability associated with orographic gradients. Ultimately, these first field campaigns were aimed at obtaining diagnostic data to guide the design of an optimal observing network including rain gauge, radars, radiosondes, and tethered balloons. First, we provide a description of the instrumentation used for the study and the conditions of the two field campaigns performed in the GSMNP during summer and fall 2008. Second, technological considerations when using multiple sensors observations and, in particular, challenges in using MRRs to estimate quantitative observations of precipitation are discussed in Section 3. Section 4 presents the results of the study with a focus on the contrasts between summer/fall and mountain/valley precipitation. Finally, the focus of Section 5 is on microphysical properties derived from MRR records.

2. Instrumentation used and data collected during the field campaigns

Two field campaigns were conducted in the GSMNP that focused on the measurement of precipitation with the double objective observing summer (warm) and fall (cold) precipitation, and to characterize the differences between mountain ridge and valley precipitation. Rain gauge records and observations from the two MRR deployments in July–August and October–November 2008 are analyzed here.

For the July deployment period (07-21-2008 to 07-31-2008), 11 rain events were recorded at the mountain ridge (Purchase Knob research station: PK). Table 1 summarizes the characteristics of each rain event. A separate rain event is defined by a minimum of three tips (i.e. a minimum of 0.3 mm) and less than 20 min between two consecutive tips. For the October–November (10-12-2008 to 11-20-2008), the number of events recorded depends on the location (mountain ridge vs. valley) and we will use ground based sensors as a reference to define the beginning and end of rain events at both locations (i.e. the rain gauge station (RG100)) deployed at Purchase Knob and an acoustic rain gauge part of a Väisälä weather transmitter (WXT510) deployed at the valley site (Haywood Community College: HCC). Based on these criteria, the rain gauge at PK (RG100) recorded 18 events, three of which were identified as snow melting as indicated by the time delay between the tips recorded by the rain gauge and the records from the collocated MRR for the same event. Finally, 15 and 10 (rain) events were recorded at the mountain ridge and the valley site that are reported in Tables 2 and 3 respectively.

2.1. Rain gauge network in the GSMNP

Starting summer 2007, a high-spatial resolution rain gauge network has been deployed in the Southern Appalachians in areas where no rainfall experiments were made previously. For the data analysis presented in this study, 20 stations equipped with tipping bucket rain gauges will be analyzed here (the current configuration of the network corresponds to about 32 stations). Rain gauges are deployed at mid to high elevations (from 1150 m to 1920 m) along exposed ridges (Fig. 1) to complement existing observations at low elevations. Seven of the rain gauges of this network are of the TB3 model with a diameter of 200 mm (i.e. 0.2 mm/tip), and 13 are of TB3/0.1 mm model with a diameter of 282.8 mm (i.e. 0.1 mm/tip). All rain gauges are regularly visited for maintenance, battery replacements, and scheduled recalibration. The rain gauges used in this study as a reference (RG100) is a TB3/0.1 mm model (i.e. 0.1 mm/tip). As mentioned earlier, a Väisälä WXT510 weather transmitter equipped with a rainfall acoustic sensor was also co-located with one of the MRRs.

2.2. Micro Rain Radar (MRR)

The microphysical observations were conducted using two vertically pointing Micro Rain Radars (MRR) operating at 24.129 GHz (K band). Drop size distributions (DSD: ND (m^{-3} mm^{-1})) can be retrieved at various heights (31 gate levels) directly overhead the deployment site. Briefly, the MRR operates under the principle of frequency modulated-continuous wave (FW-CW). The fall velocity of hydrometeors (rain, snow) leads to a Doppler shift in the received frequency in addition to the range frequency shift. The fall velocity is determined as the first moment of the Doppler spectra and the drop size distribution is determined using the relationship between the spectral reflectivity and the single particle backscattering cross section (Metek, MRR Physical Basics, 2009). One of the main limitations and expected source of errors in this method is that it does not account for vertical wind or turbulence.

From the retrieved DSD, profiles for reflectivity (Z: Eq. (1)), rain rate (RR: Eq. (2)), liquid water content (LWC: Eq. (3)) can be computed as follows:

$$Z \ (\mathrm{mm^6 \ m^{-3}}) = \int_0^\infty N(D) \cdot D^6 \cdot dD \qquad (1)$$

Table 1
Comparison of accumulated rain and average rain rate for each event observed by the rain gauge (RG100) and the MRR (MRR1) at Purchase Knob in July 2008 (warm rain only). To qualify as a separate rain event, a difference of 20 min between two rain gauge records is necessary as well as a minimum of 0.3 mm of rain accumulated (RG). For the MRR, accumulation and average rain rate are computed between the times determined by the RG.

Event PK	Start time (RG100)	End time (RG100)	RG100 (PK)		MRR1 (PK)		E (–)	EvDur (RG100) (h:min)
			Acc (mm)	AvgRR (mm h^{-1})	Acc (mm)	AvgRR (mm h^{-1})		
1	07/21 – 19:56	07/21 – 20:33	0.3	0.48	0.11	0.19	0.62	0:37
2	07/22 – 18:22	07/22 – 18:47	0.3	0.74	0.08	0.20	0.73	0:25
3	07/22 – 20:01	07/22 – 20:23	0.8	2.25	0.15	0.43	0.81	0:22
4	07/22 – 20:56	07/22 – 21:32	0.8	1.37	0.22	0.37	0.72	0:36
5	07/26 – 05:21	07/26 – 5:39	1.8	5.94	0.16	0.53	0.91	0:18
6	07/26 – 07:07	07/26 – 07:51	2.0	2.76	0.19	0.34	0.88	0:44
7	07/26 – 08:32	07/26 – 09:13	4.3	6.41	0.50	0.74	0.82	0:41
8	07/26 – 09:48	07/26 – 11:10	5.1	3.78	0.93	0.69	0.78	1:22
9	07/28 – 21:24	07/28 – 23:49	6.0	2.48	1.34	0.55	0.83	2:25
10	07/29 – 00:42	07/29 – 01:31	0.3	0.37	0.05	0.07	0.90	0:49
11	07/29 – 14:03	07/29 – 14:10	4.7	40.29	0.45	3.86	0.84	0:07
Tot. (T) or Avg. (A)	07/21 – 00:00	07/31 – 00:00	26.4(T)	**3.15(A)**	4.18(T)	**0.51(A)**	0.84	08:26(T)

$E(\%) = [AvgRR_{RG100} - AvgRR_{MRR1}]/AvgRR_{RG100}.$

$$T_{Acc}\ (mm) = \sum_{event\ i=1}^{11} Acc_i\ (mm).$$

$$A_{AvgRR}\ (mm\ h^{-1}) = \sum_{event\ i=1}^{11} AvgRR_i\ (mm\ h^{-1}) \cdot EvDur_i\ (h) \Big/ \sum_{event\ i=1}^{11} EvDur_i\ (h).$$

Table 2
Comparison of accumulated rain and average rain rate for each rain events observed by the rain gauge (RG100) and the MRR (MRR2) at Purchase Knob in October–November 2008. The same criterion to distinguish rain events than above is used as well as accumulated rain and average rain. The snow melting events were removed from the rain gauge records. E, T, and A defined in Table 1.

Event PK	Event HCC (Table 3)	Start time (RG100)	End time (RG100)	RG100 (PK)		MRR2 (PK)		E (–)	EvDur (RG100) (h:min)
				Acc (mm)	AvgRR (mm h^{-1})	Acc (mm)	AvgRR (mm h^{-1})		
1	–	10/17 – 12:42	10/17 – 13:06	0.3	0.78	0.10	0.27	0.65	0:24
2	I	10/24 – 07:16	10/24 – 09:39	2.0	0.84	2.78	1.17	−0.39	2:23
3	II	10/24 – 12:01	10/24 – 14:39	4.8	1.82	6.90	2.62	−0.44	2:38
4	III	10/24 – 16:18	10/24 – 19:37	17.4	5.24	41.41	12.46	−1.38	3:19
5	–	10/25 – 01:48	10/25 – 02:38	0.3	0.37	0.14	0.17	0.54	0:50
6	–	10/25 – 06:06	10/25 – 07:08	0.6	0.58	0.11	0.11	0.81	1:02
7	–	11/07 – 22:11	11/07 – 23:07	1.0	1.08	1.96	2.12	−0.96	0:54
8	VI	11/13 – 03:40	11/13 – 05:23	1.6	0.92	0.63	0.37	0.60	1:43
9	VI	11/13 – 06:12	11/13 – 09:47	13.2	3.69	24.51	6.86	−0.86	3:35
10	–	11/13 – 11:24	11/13 – 12:07	0.8	1.14	1.10	1.57	−0.38	0:43
11	IX	11/15 – 02:02	11/15 – 08:16	3.4	2.76	8.18	6.64	−1.41	1:14
12	X	11/15 – 06:05	11/15 – 03:33	6.5	2.64	8.25	3.35	−0.27	2:28
13	–	11/15 – 13:11	11/15 – 13:43	1.3	2.40	3.08	5.69	−1.37	0:32
14	–	11/15 – 14:25	11/15 – 14:29	0.3	4.22	1.55	21.78	−4.16	0:04
15	–	11/15 – 15:17	11/15 – 16:14	0.6	0.70	1.07	1.25	−0.79	0:57
Tot. (T) or Avg. (A)		10/12 – 00:00	11/20 – 00:00	54.1(T)	**2.35(A)**	101.8(T)	**4.50(A)**	−0.88	22:46(T)

$$R\ (mm\ h^{-1}) = \pi/6 \int_0^\infty N(D) \cdot D^3 \cdot V(D) \cdot dD \qquad (2)$$

$$LWC\ (g\ m^{-3}) = \rho_W \cdot \pi/6 \int_0^\infty N(D) \cdot D^3 \cdot dD \qquad (3)$$

where ρ_W is the density of water, and $V(D)$ is the drop fall velocity as a function of the diameter (D) according to Atlas et al. (1973) including air density variations with respect to altitude (Foote and DuToit, 1969).

For all deployments, the MRR height resolution (inter-gate distance) was selected as 150 m (i.e. covering the atmospheric column from 150 m (gate 1) up to 4650 m AGL (gate 31)), and the timescale for data averaging was 1 minute. The MRRs were deployed at two locations. The first site is in the GSMNP at Purchase Knob (PK) research station (35.586100: −83.072533: altitude 1495 m) on a mountain ridge. The second site is located lower in the valley at Haywood Community College (HCC) in Clyde (NC) (35.527150: −82.929100: altitude 803 m). Fig. 1 provides a map of the different MRR deployment sites as well as the GSMNP network. The two

sites are about 15 km apart in the NW–SE direction. For the first field campaign (July–August 2008) only one MRR (MRR1) was deployed at the first site (PK). For the second field campaign (October–November 2008), one MRR was deployed at each site (PK: MRR2 and HCC: MRR1).

3. Technical considerations and utility of the MRR

In this section, we focus on the specificity of MRR observations and challenges when comparing rain events from different sensors such as rain gauges from the GSMNP network and vertically pointing radars (MRR).

3.1. Interpreting MRR observations

Fig. 2 displays typical MRR profiles for reflectivity (Fig. 2a), fall velocity (Fig. 2b), and rain rate (Fig. 2c) recorded during the summertime deployment at the ridge site (PK). During this deployment period, eleven separate rain events that were identified from the

Table 3

Comparison of accumulated rain and average rain rate for each rain events observed by the weather station (WXT) and the MRR (MRR1) at HCC in October–November 2008. In order to keep consistency with rain gauge records, a separate rain event is defined with a maximum difference of 20 min between two WXT time stamps as well as a minimum of 0.3 mm of rain accumulated (WXT). E, T, and A defined in Table 1.

| Event	Event PK	Start time	End time	WXT (HCC)		MRR1 (HCC)		E (−)	EvDur
HCC	(Table 2)	(WXT)	(WXT)	Acc (mm)	AvgRR (mm h^{-1})	Acc (mm)	AvgRR (mm h^{-1})		(WXT) (h:min)
I	2	10/24 – 07:58	10/24 – 09:39	0.75	0.45	0.46	0.28	0.38	1:41
II	3	10/24 – 12:04	10/24 – 13:36	0.97	0.64	0.48	0.31	0.51	1:32
III	4	10/24 – 17:09	10/24 – 19:03	0.99	0.52	0.47	0.25	0.53	1:54
IV	–	11/07 – 21:17	11/07 – 21:46	0.70	1.51	0.28	0.59	0.61	0:29
V	–	11/11 – 16:52	11/11 – 16:59	0.37	3.69	0.08	0.83	0.78	0:07
VI	8–9	11/13 – 04:35	11/13 – 08:51	17.60	4.14	3.07	0.72	0.83	4:16
VII	–	11/13 – 10:38	11/13 – 11:21	0.42	0.60	0.28	0.40	0.33	0:43
VIII	–	11/14 – 18:43	11/14 – 20:13	1.47	0.99	0.43	0.29	0.70	1:30
IX	11	11/15 – 01:37	11/15 – 01:43	0.72	8.50	0.21	2.48	0.71	0:06
X	12	11/15 – 05:59	11/15 – 07:32	3.45	2.25	0.98	0.65	0.72	1:33
Tot (T) or Avg. (A)		10/12 – 00:00	11/20 – 00:00	27.4(T)	**1.96(A)**	6.74(T)	**0.50(A)**	0.75	13:51(T)
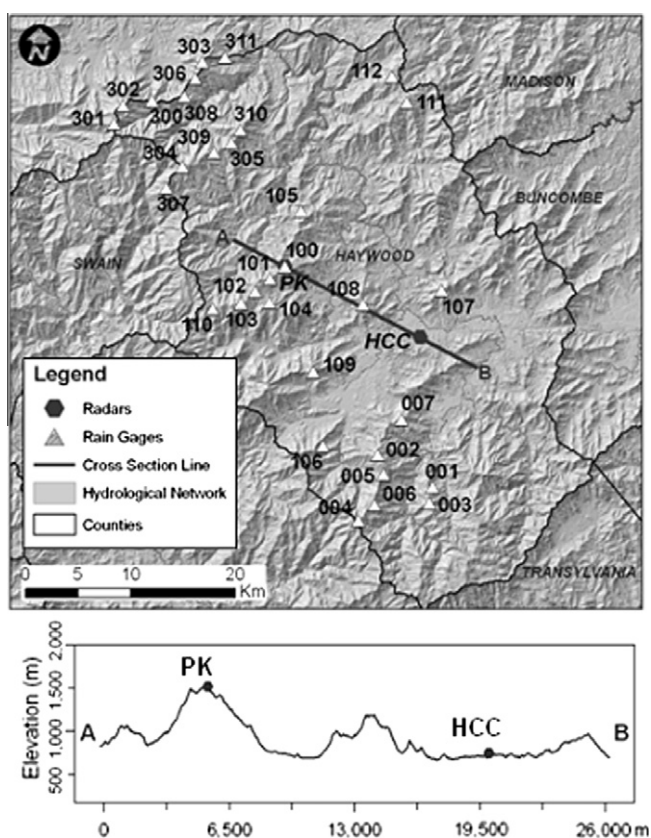
Fig. 1. Locations of the MRR deployment sites at the mountain ridge (PK) and in the valley (HCC) for summer and fall field campaigns. Locations of rain gauges constituting the GSMNP network in Haywood County, NC.

analysis of rain gauge records (Table 1), can be seen in the bottom panel of rainrate time series (Fig. 2c). A closer look at reflectivity (Fig. 2a) and fall velocity (Fig. 2b) profiles, indicates the presence of a brightband (0 °C level) located between 2500 m and 3000 m according to the radiosonde profiles.

Fig. 3 displays a comparison of two rain events recorded by both the rain gauge and the MRR for the October–November 2008 field campaign at Purchase Knob research station. Results for the MRR are presented at 600 m (gate number 4), which is one of the lowest reliable gates (Peters et al., 2005) and confirmed by analysis of the vertical profiles of rain rate and reflectivity that display a sharp, unphysical increase near the ground (first two gates) due to back-scatter effects. For the rain event on 11-13-08 (Fig. 3a), both rain

gauge and MRR time series are consistent in terms of event duration and event dynamics. For the 11-16-08 event (Fig. 3b) a precipitation event is recorded by the MRR between 21:00EST on 11-15-08 to 4:30EST on 11-16-08 while no tips were registered by the rain gauge. A closer look at the MRR time series for fall velocity (V_{fall}) and rain rate (RR) profiles (Fig. 3c and d) indicates on average a fall velocity around 1–2 m s^{-1} typical of snowfall by contrast with a fall velocity of about 3–8 m s^{-1} in the case of rain (Fig. 3d). Assuming a threshold of 0.05 mm h^{-1} to distinguish rain/no rain conditions, the rain rate time series for 11-15-08 and 11-16-08 indicates a long lasting precipitation event including a transition from rain to snow as indicated by the change in fall velocity that falls below 2.5 m s^{-1} (Fig. 3c). This value of 2.5 m s^{-1} will be used to distinguish rainfall/snow records from MRR records. Fig. 3c and d shows differences in precipitation count and characterization at the ridge and valley locations for the period 11-13-08 to 11-16-08. The rain gauge records show a delay in precipitation in the same day (11-16-08) from 11:00EST to 13:30EST due most certainly to melting of the snow accumulated in the gauge funnel earlier in the day. This example illustrates the difficulty in distinguishing rain from snow events for isolated rain gauges deployed in mountainous remote areas. Moreover, the challenge of separating rain from snow records and/or possible drizzle might induce bias but it can also affect the characterization of the diurnal cycle of rainfall that we will discuss later. In this case, the MRR collocated with the rain gauge can be of great help to separate rain from snowfall events, and to identify the transition from rain to snow which is usually challenging using the MRR alone (Cha et al., 2009).

3.2. Challenges in using MRR observations for quantitative measurements: comparison with collocated rain gauge records

Whereas the MRRs and collocated rain gauges (or acoustic rain sensor in the case of the weather transmitter) exhibit qualitatively similar skill in monitoring event duration and variation in rainfall intensity for the two deployment periods, the same cannot be said from a quantitative perspective. A comparison of MRR and collocated ground based sensors (rain gauge: RG100 or weather transmitter WXT510) measurements is presented in Fig. 4. The side-by-side comparison of the total rain accumulated during each deployment, indicates that one of the MRRs (MRR1) severely underestimates the total amount by about 600% in the summer (MRR1 vs. RG100 at PK: Fig. 4a) and by about 450% in the fall (MRR1 vs. WXT at HCC: Fig 4c). By contrast, the second MRR (MRR2) severely overestimates the total amount by about 200% (Fig. 4b). However, due to the differences in measurement sensitivity between the two MRRs and collocated ground based sensors,
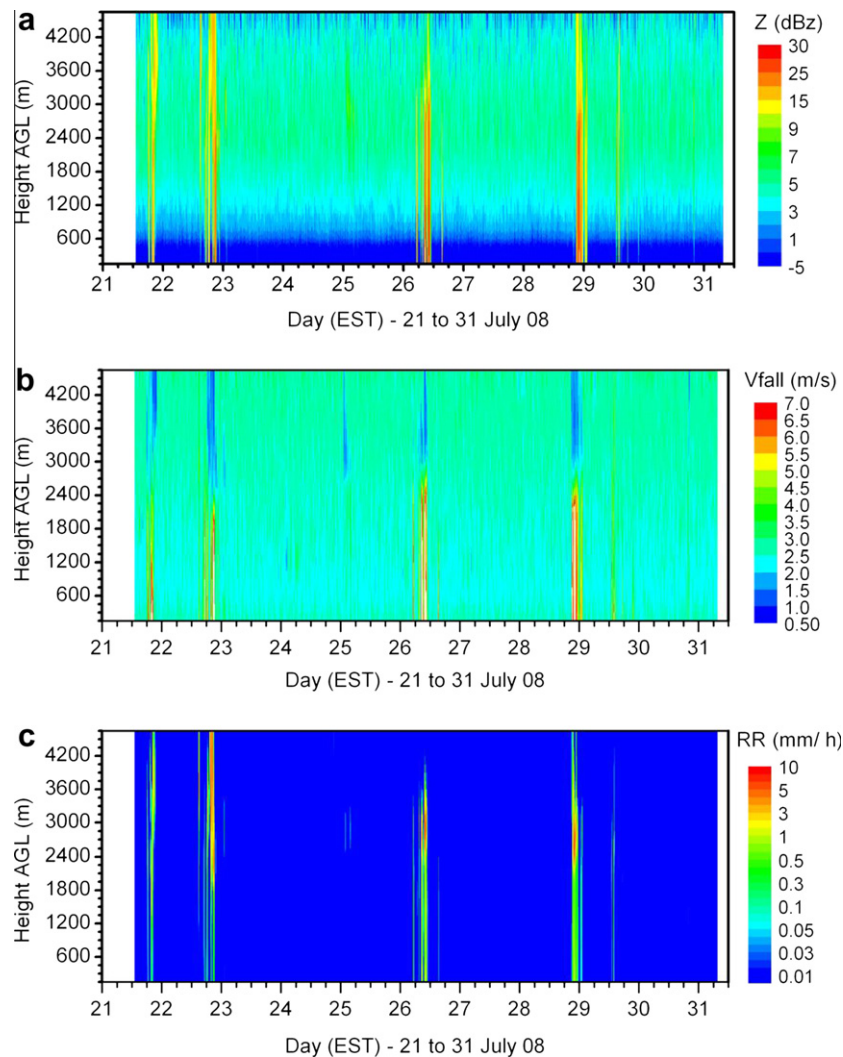
Fig. 2. MRR profiles of: (a) reflectivity (Z), (b) drop fall velocity (V_{fall}), and (c) retrieved rain rate (RR) observed during the summertime MRR deployment at the mountain ridge site (PK).

further analysis is warranted. First, the presence of snow (Fig. 3b) would introduce a non-negligible bias, as shown in Fig. 4b. Note that we reported the instantaneous intensity associated with snowfall for information purposes only and that the MRR accumulation is presented for rain records only (Fig. 4b). Second, the presence of non-precipitating clouds/fog would be accounted for in the total amount, even if they not translate into rain at the ground. Therefore, in order to determine reliable calibration coefficients, a simple comparison of the rain accumulated during each deployment is not sufficient, and an event-by-event comparison is required for each deployment. The beginning and the end of each rain event are determined using the ground sensor (RG100 or WXT) as defined in the section above. Results of the MRR/ground sensor intercomparison for summer 2008 at PK, fall 2008 at PK, and fall 2008 at HCC are reported in Table 1 (RG100 vs. MRR1), Table 2 (RG100 vs. MRR2), and Table 3 (WXT vs. MRR1) respectively. On an event-to-event basis (Fig. 4d), the total rain accumulation measured by the MRR for the same period is between 1.6 and 10 times higher for the RG100 or WXT than that for the MRR1 (Tables 1 and 3) and between three times lower and five times larger for the RG100 than that for the MRR2 (Table 2). For four events (Events #1, #5, #6, and #8: Table 2), the rain gauge accumulation is lower than retrieved by MRR2. These events are light rainfall events (RR < 1 mm h^{-1}) and differences could be due

to the limit of detection of light rainfall events by the RG100. Moreover, in addition to calibration issues mentioned previously, as the MRR internal algorithm assumes a stagnant air situation, the presence of downdrafts/updrafts (i.e. in the case of convective events) could lead to an overestimation/underestimation of the drop size and thus to an underestimation/overestimation of the rain rate (Metek, MRR Physical Basics, 2009). MRR/rain gauge intensity ratios on the order of 300% were reported by Löffler-Mang et al. (1999), and Peters et al. (2002) found a factor of 2 for single measurements between rain gauges and MRR. Therefore, it is important that prior to any MRR deployment, an on-site calibration be performed in order to adjust locally the amount of rain measured by the MRR.

Note that, even if tipping bucket rain gauges have well documented intrinsic uncertainties and biases (Ciach and Krajewski, 1999; Habib et al., 2001; Ciach, 2003; Sieck et al., 2007; Wang et al., 2008), these uncertainties appear to be well below the variability associated with MRR measurements (Löffler-Mang et al., 1999; Peters et al., 2002). Another source of uncertainty relates to the presence of recurrent fog, drizzle, and low level clouds that constitute an important part of the water cycle in the Great Smoky Mountains. For instance, the MRR can detect rain rates as low as 0.01 mm h^{-1} but the RG has a threshold of 0.1 mm h^{-1} (i.e. less than 1 h between two consecutive tips of 0.1 mm). The weather
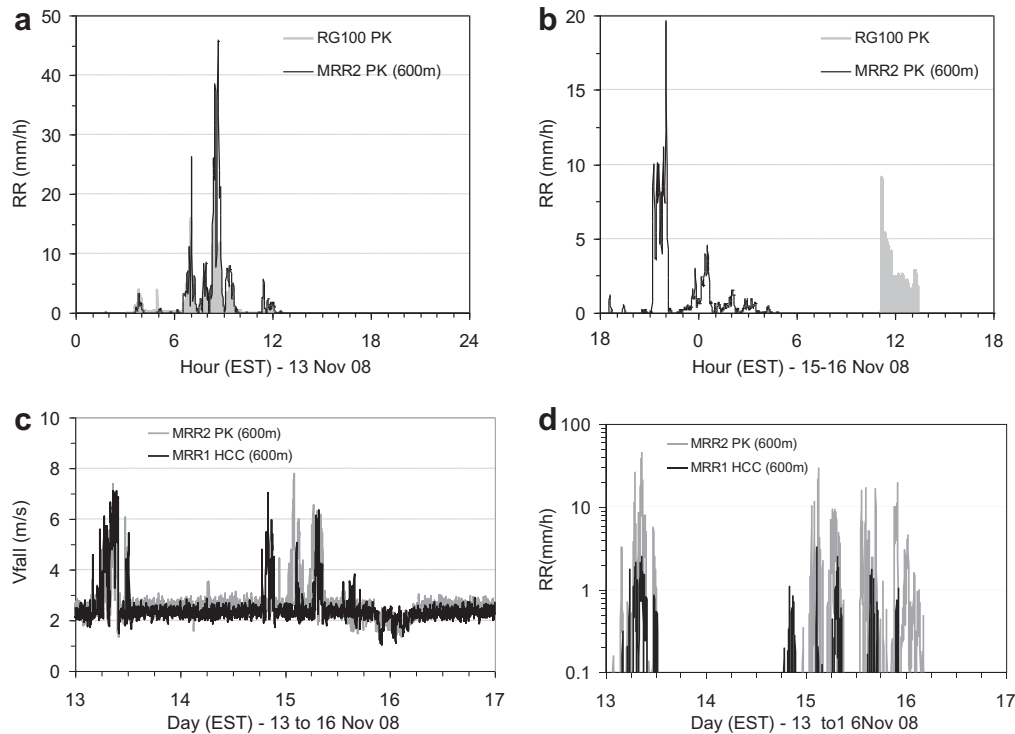
Fig. 3. Rain rate comparison between rain gauge (RG100) at ground level and collocated MRR at the mountain ridge site deployment (PK): (a) for 11-13-08, (b) for 11-15/16-08 (snow conditions). MRR time series for the period 13-16 November 2008 at both locations: (c) fall velocity, (d) rain rate.

transmitter has a similar threshold of 0.1 mm h^{-1}. Additional tests performed for the same rain event (not shown), indicated a difference of about 10% in terms of the accumulated rain between the weather transmitter (WXT510) and a rain gauge (TB3) similar of RG100. This difference between WXT510 and RG is on the order of magnitude expected with two collocated rain gauges (Sieck et al., 2007).

Based on the rain events summarized in Tables 1–3, the values of the MRR adjustment coefficients determined using a time weighted average of the rain intensity to account for each event duration and respective contribution (Tables #1, #2, and #3). Calibration coefficients for each deployment period are K_1 = 6.15 (=3.15/0.51), K_2 = 0.52 (=2.35/4.50), and K_3 = 3.98 (=1.96/0.50) respectively. For the remaining of this work, we rely on RG and WXT records of total rainfall, rainfall intensity, and event duration to adjust MRR records (accumulated rainfall, average rain rate) using the coefficients valid for each MRR deployed.

4. Analysis of the intense observation periods (IOPs)

In this section, the focus is first on the seasonal contrast between summer (July–August) and fall precipitation (October–November) in the inner region of the GSMNP, and second on the ridge-valley contrasts including differences in the diurnal cycle at both locations.

4.1. Seasonal variability

Fig. 5 displays the diurnal cycle of rainfall on a 3-h basis. The 3-h period was selected to achieve robust statistics. For summertime precipitation we selected a time period of 3 months starting with the initial rain gauge installation date (06-01-08 to 08-31-08). For fall records we selected the period (10-12-08 to 11-20-08) when the MRR was deployed to distinguish unambiguously melting of snow accumulation in the gauge funnel from actual rainfall. Fig. 5a displays the diurnal partition of the 1200 tips recorded by

the rain gauge during the first observation period (06-01-08 to 08-31-08) and the 650 tips (750 tips including snow melting records) for the second period (10-12-08 to 11-20-08). During the summer, nighttime and early morning precipitation (0:00EST to 9:00EST) amounts to 5% and 10% of the total, in the remainder of the day 3-h rainfall frequency accounts for about 15–20% and remains more or less uniform throughout the day (9:00EST to 24:00EST) (Fig. 5b). During the fall, nearly half of the precipitation (46%) occurs in the afternoon (12:00EST to 18:00EST), and only 10% takes place at night (21:00EST to 6:00EST). Rainfall intensity in the fall (~1.5–4 mm h^{-1}) is characteristic of stratiform rainfall regardless of the time of the day (Fig. 5c). Rainfall intensity is systematically higher in the summer (>4 mm h^{-1}) except during the early morning period (3:00EST to 6:00EST), whereas intense rainfall (>10 mm h^{-1}) was recorded only in the afternoon (15:00EST to 18:00EST) associated with convective activity including isolated mountain thunderstorms. The apparent differences between the summertime diurnal cycle of rainfall intensity based on rain gauge records (Fig. 5c) and the MRR (Table 1) are attributed to the relative short duration of the MRR deployment period: that is, 3-months (June–July–August) vs. 10-days IOP (07-21-08 to 07-31-08). Consequently, the 11 events occurring during the 10 days of the MRR deployment (Table 1) are not expected to capture the seasonal statistics. Furthermore, in the description of rain gauge records, we consider rain gauge tips occurring over fixed 3-h periods regardless of the beginning and ending time of specific events. Nevertheless, two events (#6 and #8 in Table 1) are representative of summer precipitation events with comparable rainfall intensity derived from rain gauge records (Fig. 5c) and MRR observations (Table 1). We note that Event #11 (Table 1) that corresponds to a very short afternoon convective event, if representative of afternoon thunderstorms in the area, display an average rain rate about 4-fold the average rain rate computed for the whole 3-months.

Rain gauge records at PK (ridge site) show that the summer season is overall dry (rainfall was detected only 5% of the time), and
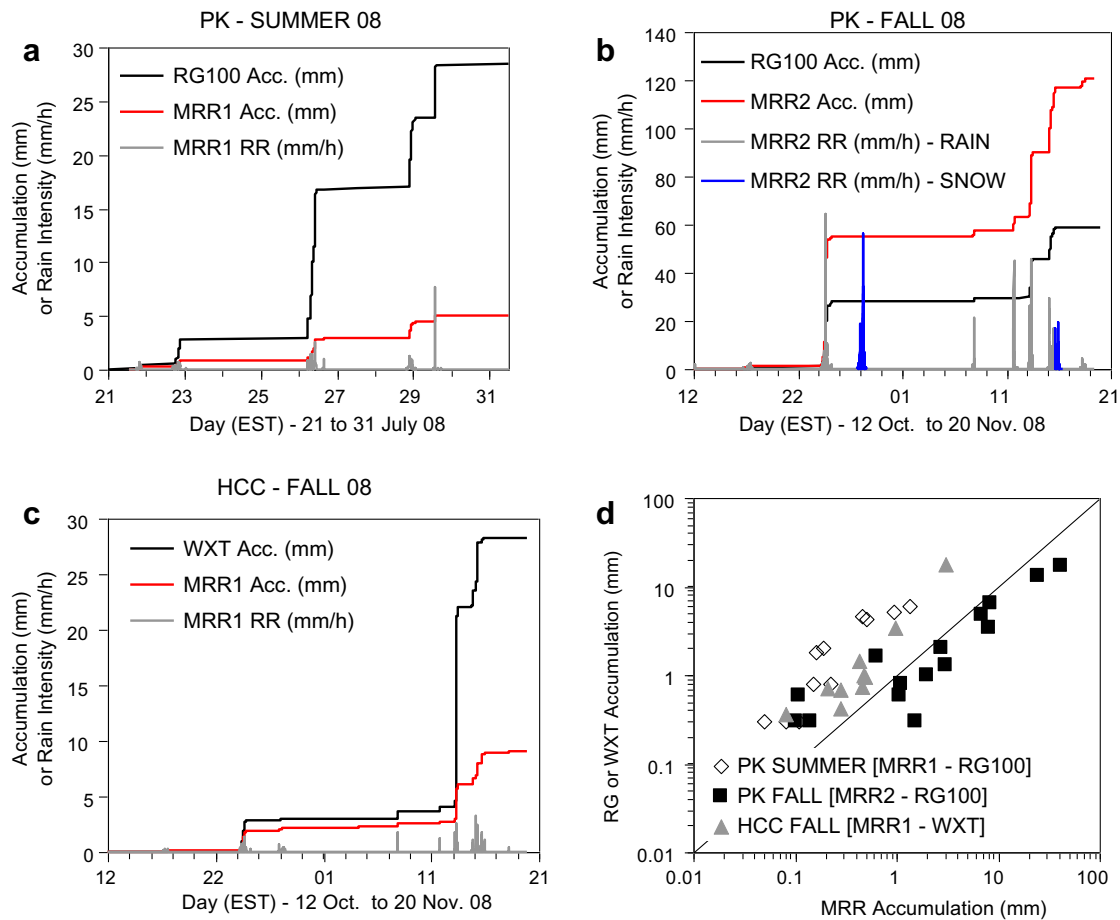
Fig. 4. Comparison of accumulated rain between each MRR at 600 m and the collocated sensor taken as a reference at ground level: (a) July 2008 (MRR1 and RG100) at PK; (b) October–November 2008 (MRR2 and RG100) at PK; (c) October–November 2008 (MRR1 and WXT) at HCC; and (d) event-by-event accumulation comparison for all deployments. The instantaneous rain intensity retrieved by each MRR is also reported. For the deployment in October–November 2008, only rain records are accounted in the total used for MRR calibration. The snow event intensity (blue) is reported for illustration purposes only. (For interpretation of the references to colour in this figure legend, the reader is referred to the web version of this article.)

although heavy convective rainfall was recorded only sporadically (4% of the total duration), it contributed 41% (82 mm) of the total rainfall accumulation (200 mm). For the two observation periods, the average daytime accumulation is about 25% higher for the summer season (i.e. average of 2.2 mm/day for June–August) as compared to the fall (i.e. average of 1.75 mm/day for October–November) (Fig. 5d). In both cases, 60% of the total accumulated rainfall is produced in the afternoon through the evening (12:00EST to 21:00EST). The main differences between the two periods are in the relative contributions to the diurnal cycle of early morning (6:00EST to 9:00EST) and nighttime rainfall contributions: the rainfall accumulation represents 7% of the daily total in summer as compared to 21% for fall in the early morning, and at nighttime 22% of daily total precipitation for summertime and 11% for fall. A more complete analysis of the seasonal cycle will be conducted in the future as more data become available.

4.2. Ridge- valley contrast and evidence of orographic enhancement

For the second field deployment in October–November 2008, two MRRs were deployed at the mountain ridge site (PK) and in the adjacent valley (HCC) at Clyde (NC). In order to compare rain duration at both locations during the entire fall deployment period, we use MRR records that are more sensitive to low rainfall intensity than the rain gauge or the weather transmitter (0.1 mm h^{-1} for the RG TB3/0.1 mm and the WXT510) with 1 min time-steps. Moreover, MRR records allow to distinguish

precipitation types; rainfall (i.e. time stamps with RR > 0.05 mm h^{-1} and V_{fall} > 2.5 m s^{-1}) and snow/mixed rain (i.e. time stamps with RR > 0.05 mm h^{-1} and V_{fall} < 2.5 m s^{-1}).

Fig. 6a displays the precipitation duration at both locations as a function of the elevation for the portion of the atmosphere directly overlooking each MRR deployment site from 150 m AGL up to 4650 m AGL. Both profiles display a decrease in precipitation detection with increasing height. Due to the fact that low to moderate intensity events account for most of the precipitation, the increasing detection threshold with increasing distance from the radar could partially explain this shape. In addition, since this trend is particularly pronounced at the mountain ridge (PK) for altitudes above 2600 m AGL, another possible factor of influence is the presence of recurrent fog, drizzle, and low level clouds. Logically we note the absence of rain records for altitudes above 2600 m AGL; that is above the freezing level. Considering the lowest reliable MRR gates (MRR gates 3–4: i.e. 450–600 m AGL), the duration of precipitation is about 3.2 times higher at the mountain ridge than in the valley, with about 6.8% of the total deployment duration at PK and 2.1% at HCC. For rainfall only, this duration is about the double at PK (29:45 h) than at HCC (15:55 h). Differences with the total duration of the rain events measured at both locations in Tables 2 (22:46 h at PK) and 3 (13:50 h at HCC), are explained by the fact that the MRRs are more sensitive to low rainfall intensity (RR ≈ 0.05 mm h^{-1}), and that only significant rain events (total rainfall > 0.3 mm) were reported for the RG and the WXT (Tables 2 and 3). Note that this difference MRR/ground
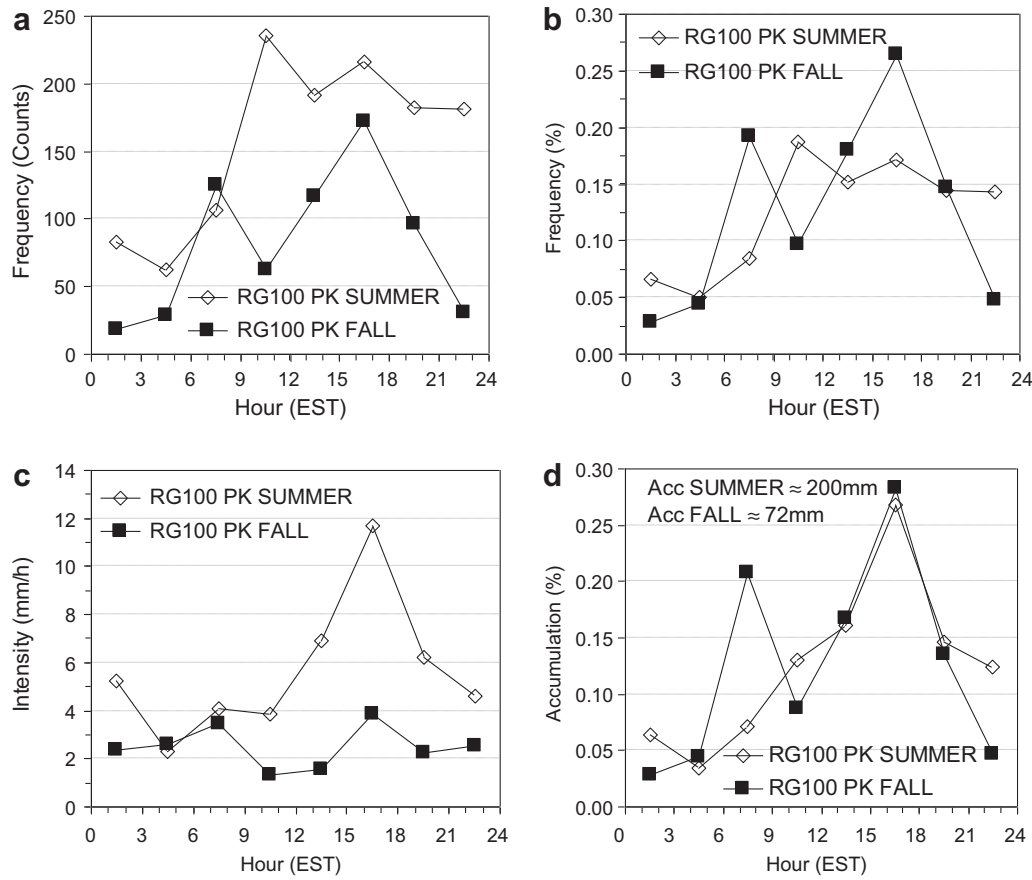
Fig. 5. 3-h period diurnal cycle of precipitation at the mountain ridge (PK) recorded by the rain gauge (RG100) in the summer (June, July and August 2008) and fall period (October, November 2008): (a) frequency in terms of tips recorded, (b) frequency in terms of percentage, (c) average rain rate, and (d) accumulation. For fall, the records identified as snow melting events are removed from the RG records for the diurnal cycle calculation. However, the total accumulated (≈72 mm) includes both rain and snow melting events.

based sensor is about 30% at PK (15% at HCC), and is consistent with the frequent presence of fog/drizzle at higher elevations in the GSMNP.

A similar trend is found for precipitation accumulation with an estimated amount of rainfall measured at PK (the ridge site) about twice the amount measured at HCC (the valley site) (i.e. measured total of 54.1 mm at PK vs. 27.4 mm at HCC for rain records only). This result is further confirmed by a comparable average rain rate (within 12%) at the valley site (HCC) and the mountain ridge (PK) for the lower atmospheric domain (Fig. 6b). This difference in terms of cumulative precipitation reduces to 60% when considering concurrent precipitation defined from rain gauge records at PK and weather transmitter records at HCC with a total of 41.3 mm at PK (ridge) vs. 25.9 mm at HCC (valley). This corresponds to an orographic "enhancement" between the mountain ridge and the valley of about 60% on an event basis, leading up to 100% at the seasonal scale.

For concurrent events (Fig. 6c), the difference in terms of rain rate retrieved at each location near the surface (AGL) reduces to about 30% (the ridge site having the higher intensity) and can be explained by the fact that rainfall, indeed light rainfall, is significantly more frequent at high elevation. Furthermore, we note that the difference in term of intensity the same elevation above sea level (ASL) is very small (<5%) (Fig. 6c). The close match of PK and HCC MRR vertical profiles observed ASL for concurrent rain events is consistent with local homogeneity of atmospheric conditions in the case of large scale systems. This instills confidence in the adjustments of MRR records from rain gauge measurements, and

therefore illustrates the necessity to perform careful adjustments of raw MRR data in order to obtain skillful quantitative precipitation estimates. For instance, the use of raw MRR records without local calibration would indicate 21 (entire period of deployment) and 11 (at both locations simultaneously) times more precipitation at PK than at HCC.

The diurnal cycle obtained with the MRRs located at PK and HCC (Fig. 7) exhibits roughly similar shapes when compared to the diurnal cycle obtained with the rain gauges (Fig. 5). For an easier comparison between geographical locations, the frequency for MRR records is expressed in percent with respect to the total number of time stamps for snow/mixed rain or rainfall. Regardless of precipitation type (rainfall/snow) and deployment location, more than 50% of the events occur at nighttime and early morning (0:00EST to 9:00EST) (Fig. 7a and b), with about 40% between 6:00EST and 9:00EST at HCC (Fig. 7b). However, if a distinction is made between MRR records for snow/mixed rain and rainfall, most of the nighttime and early morning events (21:00EST to 6:00EST) at PK (Fig. 7c) are identified as snow. This distinction between rain and snow is less significant for valley records due to the predominance of rainfall (Fig. 7d) with the relative duration of snow 20% of the time at HCC and 50% at Purchase Knob, corresponding respectively to 10% and 30% of the total precipitation corrected accumulation at each location. Further evidence of valley-ridge contrasts are found in late afternoon precipitation (15:00EST to 18:00EST) with high rainfall intensity which is less frequent in the valley (Fig. 7b) than on the ridge (Fig. 7a); thus emphasizing the influence of the landform in organizing afternoon orographic enhancement at higher elevation.
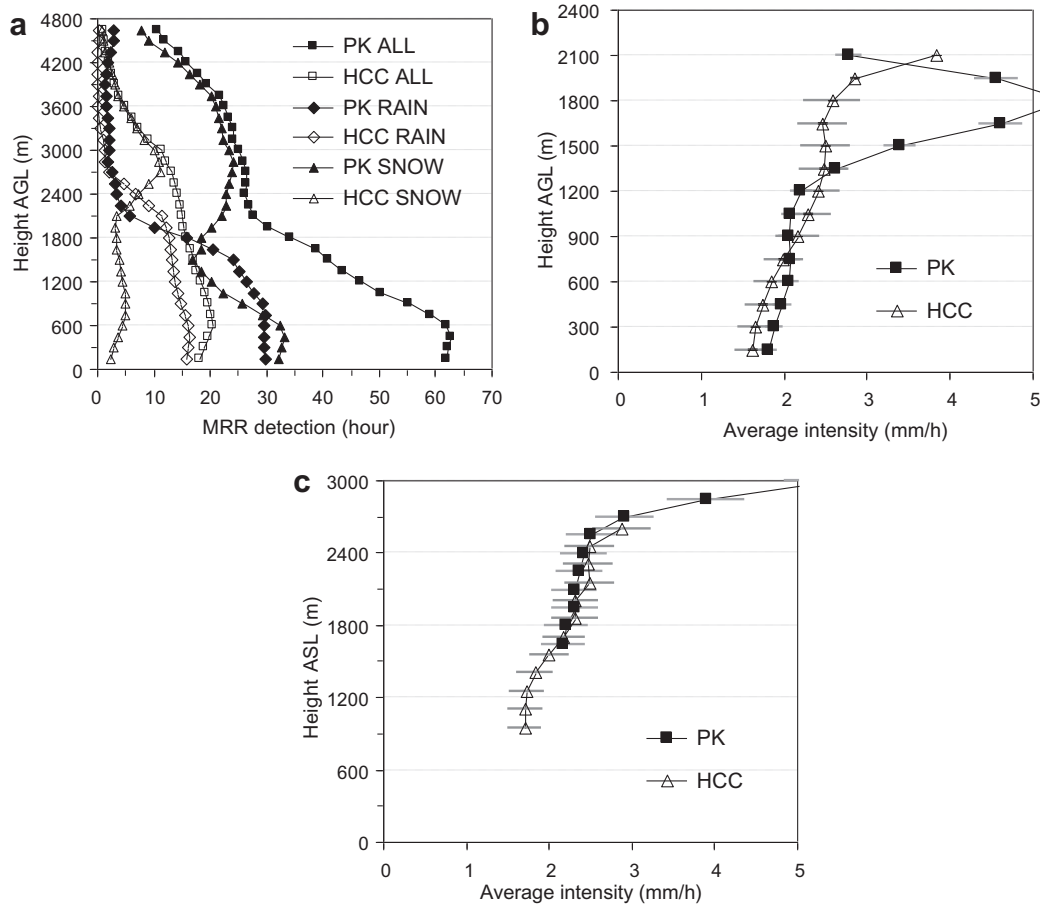
Fig. 6. (a) Rain detection at both locations HCC (valley) and PK (mountain ridge) during the MRR deployment from 10-11-08 to 11-20-08 as a function of the elevation above ground level (AGL). Adjusted average rain intensity: (b) for each site (PK and HCC) independently of the other (HCC and PK) as a function of the elevation AGL, and (c) for each site (PK and HCC) and for concurrent events as a function of the elevation above sea level (ASL). In order to achieve robust statistics, average intensities are computed using a threshold of 0.5% for the detection level (5 h).

In the early morning (6:00EST to 9:00EST) rainfall intensity in the valley (HCC) is higher than during the rest of the day and higher than the intensity in the ridge (PK) at the same time (Fig. 7e). Furthermore, the morning maximum observed at HCC (2.6 mm h^{-1}) is less intense (100%) than the afternoon maximum at PK (5.3 mm h^{-1}). Note that in term of rain accumulation, comparable amounts (within 15%) are retrieved for the early morning (6:00EST to 9:00EST) at both locations while a 5-fold difference (the ridge site being the highest) is obtained for the late afternoon (15:00EST to 18:00EST) (Fig. 7f). Regardless of the location, rain

(Fig. 7f) is equivalent to the double peaked curve observed with the rain gauge (Fig. 5).

In order to investigate the relationship between the time series for integral parameters recorded by the two MRRs (reflectivity and rain rate), spacio-temporal correlations were computed. With a time lag of ±60 min between PK and HCC reflectivity records (a positive time difference indicating that PK records are ahead when compared to HCC records), cross-gate correlations were computed for each rainy day and for selected rain events. The correlation factor is defined as follows:

$$R_{jPK\_iHCC}(t + \Delta t) = \frac{N\sum_N Z_{jPK}(t + \Delta t) \cdot Z_{iHCC}(t) - \sum_N Z_{jPK}(t + \Delta t) \cdot \sum_N Z_{iHCC}(t)}{\sqrt{N\sum_N Z_{jPK}^2(t + \Delta t) - \left(\sum_N Z_{jPK}(t + \Delta t)\right)^2} \cdot \sqrt{N\sum_N Z_{iHCC}^2(t) - \left(\sum_N Z_{iHCC}(t)\right)^2}} \qquad (4)$$

events (Fig. 7f) dominate in the early morning (6:00EST to 9:00EST) and late afternoon (15:00EST to 18:00EST) similar to those recorded with the rain gauge for the same location deployment period (Fig. 5d). At higher elevation, MRR records for rainfall evolve from a large number of counts (Fig. 7a) at low-moderate intensity (Fig. 7e) for the early morning (6:00–9:00) to a smaller number of counts (Fig. 7a) with an increase in rainfall intensity (Fig. 7e) for the afternoon (15:00–18:00). In term of rainfall accumulation, the diurnal cycle obtained with MRR records at PK

Records that include rainy and non-rainy records (not shown) display a correlation coefficient ranging from 0 to 0.4 (at $\Delta t = -60$ min) to 0.3 to 0.7 (at $\Delta t = -20$ min to +20 min) and back down to 0 to 0.4 (at $\Delta t = +60$ min). The maximum correlation coefficients (Eq. (4)) are found for $\Delta t = -10/+10$ min and along the line $j_{GATE\_PK} = i_{GATE\_HCC} + 5$ which corresponds approximately to the difference in elevation (692 m i.e. $\approx 4.6 \times 150$ m) between the two sites. We note that for concurrent rain events (i.e. both MRR rain rate records simultaneously non-null), the maximum
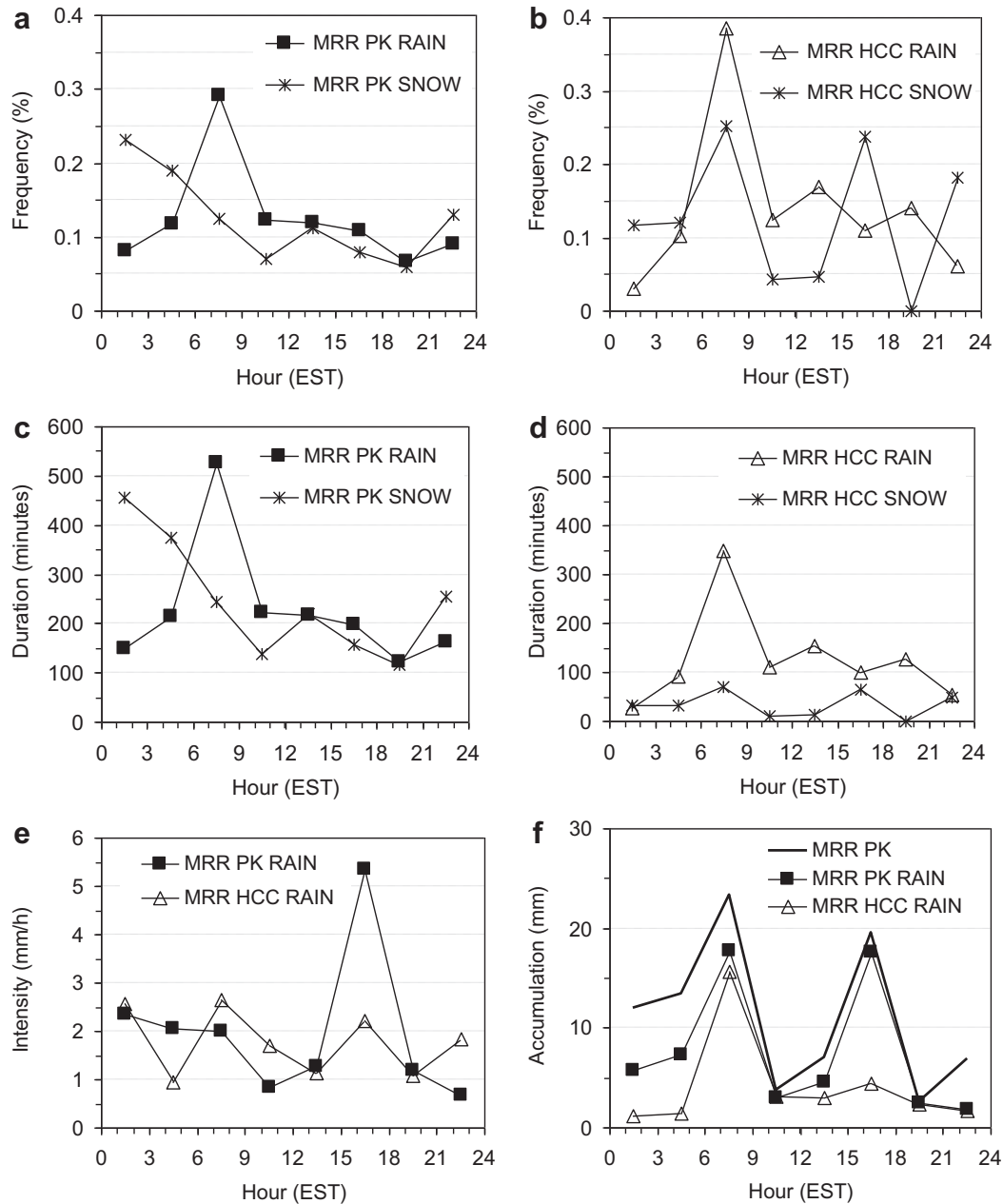
Fig. 7. Diurnal cycle of precipitation at the ridge (PK) and valley (HCC) locations recorded by the two MRRs for the fall period (October, November 2008), for all events (rain + snow). Event frequency in terms of percentage: (a) PK and b) HCC. The frequency (%) is defined as the number of MRR records for which RR > 0.05 mm h^{-1}. We distinguish rain (RR > 0.05 mm h^{-1} and V_{fall} > 2.5 m/s) and snow (RR > 0.05 mm h^{-1} and V_{fall} < 2.5 m/s). Event duration in terms of minutes: (c) PK, (d) HCC, e) intensity at PK and HCC, and (f) accumulation at PK and HCC. For PK, total water accumulated (rain + snow) are displayed for comparison.

correlation coefficient of 0.7 is found at a height of about 1200–1500 m AGL (with respect to the mountain ridge site: PK) and corresponds to the brightband location in the MRR reflectivity profiles. In addition, when correlations are computed using all rainy day records for the period of deployment (i.e. MRR records for which rain rate values are non-null), the maximum correlation coefficients are found for $\Delta t \approx$ + 10 min that is rainfall arrives earlier at PK (ridge) relative to HCC (valley). Considering their relative positions in the context of the surrounding terrain (HCC is located roughly 15 km E–SE of PK, Fig. 1), these results are consistent with rainshadow effects. However, results can be different when correlations are computed for selected episodes depending on where the storm systems are coming from.

Fig. 8 displays cross-gate correlations for three different episodes on 10-24-08: (1) early morning (6:00EST to 10:00EST:

Fig. 8 – left column), (2) early afternoon (11:00EST to 15:00EST: Fig. 8 – med column), and (3) late afternoon (16:00EST to 20:00EST: Fig. 8 – right column). See also Tables 2 and 3. On a gate-by-gate basis, the behavior of the correlation coefficient is difficult to interpret. For instance, for the first event (Fig. 8a), we observe that maximum correlation values are organized along the line corresponding to the same elevation ($H_{HCC} = H_{PK}$). For the second event (Fig. 8b), a horizontal threshold is observed around gate 15 at PK (corresponding to 2250 m AGL), while a localized maximum is present between gates 20–25 at HCC (between 3000 and 3750 m AGL). Yet, the vertical profile of rainfall detection (Fig. 6a) shows that at these heights rain detection is very weak. Additionally, both domains correspond to the upper atmosphere above the brightband for which retrieval of the DSD and related integral properties are less reliable (Fig. 6b). Because the correla-
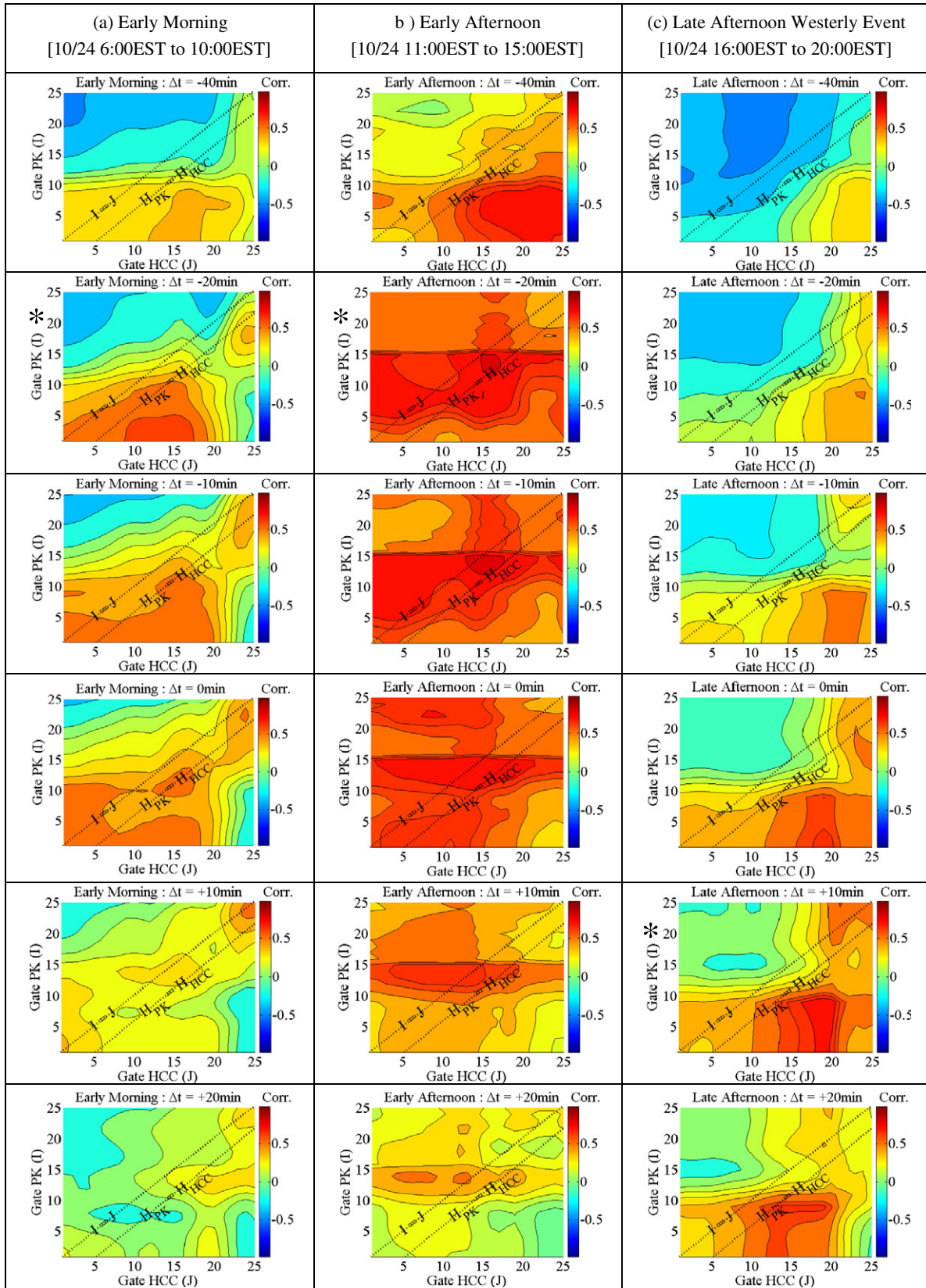
Fig. 8. Space–time correlation coefficient between the reflectivity time series of the two MRR: MRR1 (HCC) and MRR2 (PK) as a function of gate number and for different values of the time difference (Δt = −40-, −20-, −10-, 0, +10-, +20-min). For all Z records: (a) 10-24-08 6:00EST to 10:00EST. (b) 10–24–08 11:00EST to 15:00EST. (c) 10–24–08 16:00EST to 20:00EST. Doted lines indicate similar gates (I = J) and similar elevation ($H_{PK} = H_{HCC}$) at both sites. The star indicates the approximate value of Δt corresponding to the maximum correlation.

tions were computed for the entire period of record (and not limited to non-null records only), a possible explanation could be that these thresholds are a signature of the transition from rain/ice domain above the freezing level and, or artifacts caused by the decrease in rain detection threshold with increasing distance from the radar. Focusing on the lower troposphere where correlation values are statistically meaningful and limited to warm rain, for the first two episodes (1) and (2) (events #2 and #3 in Table 2 and events #I and #II in Table 3) the maximum correlation is found for negative values of $\Delta t = -25/-15$ min (1st column, second figure from the top: maximum correlation >0.6) and $\Delta t = -30/-10$ min (2nd column, second figure from the top: maximum correlation >0.8), with HCC reflectivity records ahead of PK. That is, storm systems came from HCC (valley) and later moved to PK (ridge). The opposite happens for the third episode, in the late afternoon (3rd column: event #4 in Table 2 event #III in Table 3), the maximum correlation is found for positive values of $\Delta t = +5/+15$ min (third column, fifth figure from the top: maximum correlation >0.7).

Further insight can be obtained from reviewing NEXRAD national mosaic reflectivity images from the National Climatic Data Center (NCDC). Hourly composite images for the continental United States are available at (http://www4.ncdc.noaa.gov/cgi-win/wwcgi.dll?WWNEXRAD~Images2. The two closest WSR-88D NEXRAD radar stations to the study area are located in Knoxville, TN (KMRX: 36.169, −83.402, altitude 407 m) about 71 km in the NW direction from PK, and in Greer, SC (KGSP: 34.883, −82.22, altitude 286 m) about 110 km from PK in the SE direction. The areal coverage of both radars is strongly affected by mountain blocking (Miller et al., submitted for publication). NEXRAD images on 10-24-08 show the presence of two precipitation systems: a SWesterly system (S1) originating from the Gulf of Mexico at 0:00EST, and a Westerly system (S2) that crosses the Appalachians. The two first precipitation episodes (Table 2: #2 and #3 and Table 3: #I and #II) in the early morning and the early afternoon are related to the first southwesterly precipitation system (S1) as it reaches the MRR deployment area around 6:00EST. For those two episodes, the orographic configuration of MRR deployment area (Fig. 1) can explain the fact that MRR records at HCC are in advance when compared to MRR records at PK. Despite the fact that the precipitation system direction is almost perpendicular to the MRRs deployment sites located along a NW–SE direction, the time difference corresponds to the propagation time of the southwesterly system (S1) from the valley site to the ridge site due to interaction with the terrain which causes it to propagate inward at a slower pace along against the ridge. Please note that the apparent discrepancy for the chronology of rain events defined by ground sensors (RG/WXT) and by the analysis of spatial-temporal cross correlations computed from MRR reflectivity records (i.e. RG records for

events #2 and #3 in Table 2 (PK) starting earlier than WXT records for corresponding events #I and #II in Table 3 (HCC)) can be explained by the definition of a rain event for the purposes of this study (i.e. minimum of 0.3mm and less than 20 minutes between two records, which rules out earlier WXT records) and by MRR reflectivity records that might correspond to non-precipitating conditions, in particular at the beginning of the rain event when storm systems move over the area of observation. The late afternoon precipitation event (Table 2: #4 and Table 3: #III), corresponds to the second westerly precipitation system (S2), which reaches the area around 16:00EST with MRR records from PK in advance when compared to HCC records. The comparison of the cumulative precipitation recorded at the ground at the two locations (24.2 mm [Table 2: #2 + 3 + 4] at PK and 2.7 mm [Table 3: #I + II + III] at HCC) shows that for this particular day the orographic enhancement effect is on the order of ninefold between the "upstream/upwind" and "downstream/downwind" locations. The ability to diagnose such large differences in rainfall totals is critical in this region of the Appalachians, which is plagued by the occurrence of landslides and debris flows with origination points at upslope locations geomorphically similar to PK (Wooten et al., 2008).

5. Microphysics

5.1. MRR DSD retrieval

The DSDs produced by the MRR retrieval algorithm are displayed in Fig. 9. For that purpose, we display the normalized DSD at 600 m to compare the shape of the DSD regardless of radar calibration considerations (see Section 3.1). A comparison of the shape of the normalized DSD between summer and fall shows without ambiguity important differences for DSD retrieved at the higher elevation deployment site (Fig. 9a). Summer drop spectra (520 spectra) exhibit a heavier right tail (minimum slope $\Lambda = 16$ cm^{-1}) than fall spectra (2824 spectra: minimum slope $\Lambda = 25$ cm^{-1}), thus an increased number of larger drops. For low to moderate rain intensity (<20 mm h^{-1}), which is the case for all the rain events reported here, Prat and Barros (2009) showed that coalescence is the dominant microphysical process. The heavier DSD tail for larger drop sizes results from enhanced coalescence efficiency, and this suggests that the dominant microphysical mechanism of orographic enhancement is coalescence. For instance, events #9 and #11 (Table 1) were without doubt associated to localized embedded convection centered over the deployment site at PK (Miller et al., submitted for publication). Another possible explanation could be that the summertime bright-band level is higher (2400–2600 m AGL at PK) in comparison to fall (around
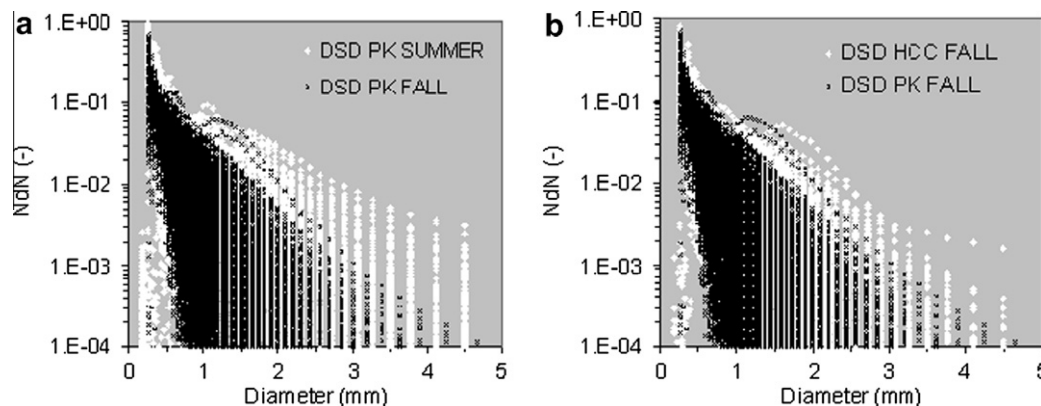

Fig. 9. Normalized DSD retrieved with the MRR: (a) comparison between summer and fall deployments at PK and (b) comparison between PK and HCC during the fall deployment. Both cases are for rain records only.

1100–1300 m AGL at PK), and thus an increased fall distance in summer could lead to an enhanced coalescence process due to the higher probability of drop–drop interactions.

Despite the small number of summertime rain events at PK (Table 1), the data show a strong seasonal signature for the microstructure of precipitation. Smaller differences were observed during fall deployment at both locations as compared to summer. Indeed DSDs for higher (PK: 2824 spectra) and lower (HCC: 924 spectra) elevations, occupy approximately the same parameter space with some DSDs recorded at the valley site (HCC) exhibiting a heavier tail than DSDs recorded at higher elevation (Fig 9b). Again, given that the 0 °C isotherm is higher at HCC than at PK, a higher fall distance over the lower elevation site HCC would increase the probability of drop–drop interactions and possibly enhance the coalescence mechanism resulting in the creation of bigger drops as predicted elsewhere for the rain rates observed (RR < 20 mm h^{-1}) (Prat and Barros, 2009). However, the differences observed do not seem statistically meaningful to draw definitive conclusions at this point.

5.2. MRR DSD ambiguity

The MRR microphysical data, specifically the DSDs, were used to derive boundary conditions to drive a rainshaft microphysical model (Prat and Barros, 2007a,b) in order to improve the estimation of surface rain rates and to assess the dynamics of DSD evolution with height and with time. This was done previously by Prat et al. (2008) for a vertically pointing radar and Prat and Barros (2009) using satellite observations from the Tropical Rainfall Measurement Mission Precipitation Radar (TRMM PR). In particular, Prat et al. (2008) showed that as long as a top boundary condition

can be defined where high accuracy measurements are available, the column microphysical model can produce surface rain rate estimates very close (~5% difference) to those obtained using rain gauges and disdrometers. Here the model is used as a reverse analysis tool to investigate the internal consistency of MRR observations and derived products, especially with regard to the microphysics.

Fig. 10 displays the intercomparison of ground based rain gauge measurements, MRR records at 600 m, and surface rain rate simulated by the model using MRR observations as boundary conditions for two selected events during the summer (Fig. 10a–c: 07/29/08) and fall deployments (Fig. 10b–d: 11/13/08). Two types of DSDs were used: (1) DSDs directly retrieved by the MRR as discussed in Section 5.1, and (2) Marshall-Palmer DSDs (1948: hereafter MP48) that were derived from MRR reflectivity (Z) measurements. Rain events were simulated by imposing 1-min time series DSD as dynamical boundary conditions at the top of the rainshaft (Prat et al., 2008). The rainshaft height was selected for conditions free of ice particles (warm rain) and corresponds to the first or second gate below the location of the maximum reflectivity (brightband).

A comparison of MRR DSDs with MP DSDs derived from MRR reflectivity (Z) measurements that are used as boundary conditions for the microphysical model is presented in Fig. 11. In terms of accumulated rain, the comparison of MRR time series at 600 m with rain gauge records indicates a relative difference of −75% (MRR1: Fig. 10c) and up to +90% (MRR2: Fig. 10d) respectively. For the summer case (Fig. 10c), the difference between model results and rain gauge data is about −55% when using the MRR DSDs at a fixed height (2250 m AGL) as boundary conditions for the microphysical model, and −70% with DSDs derived from MRR reflectivity (Z at 2250 m AGL). For the dynamic modeling of
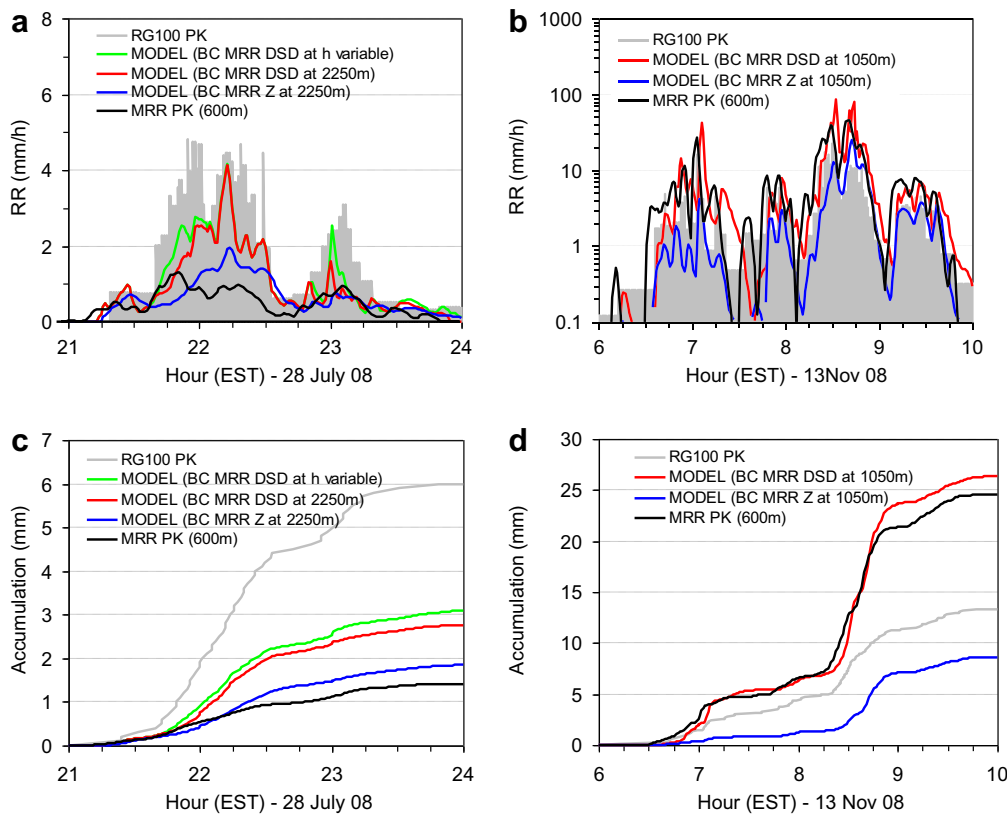

Fig. 10. Intercomparison of rain gauge records (RG100 PK) and MRR time series (MRR PK) with modeling result obtained at ground level. For the rain rate: (a) 07-28-08 (MRR1) and (b) 11-13-08. For the rain accumulated: (c) 07-28-08 and (d) 11-13-08. DSDs at selected heights are used as boundary conditions for the model with DSDs at 2250 m (07-28-08) and at 1050 m (11-13-08). Rain gauge rain rates are 1 min average.
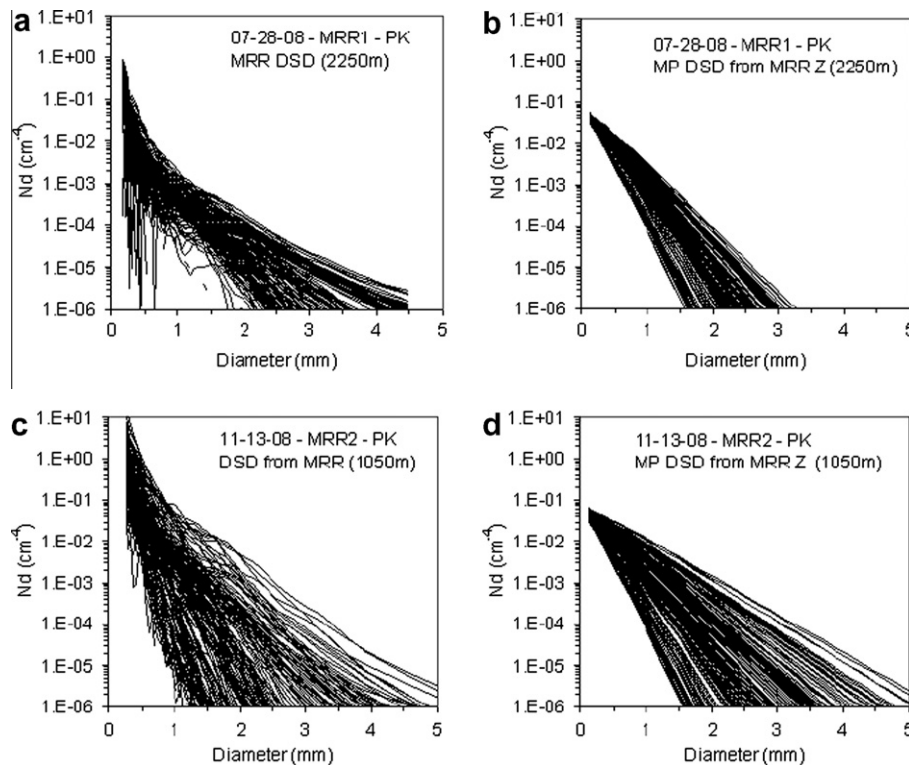
Fig. 11. DSDs used as boundary conditions in the microphysical model. (a) DSD at 2250 m from the MRR on 07-28-08, (b) MP DSD from MRR reflectivity at 2250 m on 07-28-08, (c) DSD at 1050 m from the MRR on 11-13-08, and (d) MP DSD from MRR reflectivity at 1050 m on 11-13-08.

summertime rainrate (moderate RR ≈ 2.5 mm h^{-1}: Table 1 – Event #9), a significant improvement (−55% vs. −70%) is obtained with the microphysical model using MRR DSDs (at 2250 m AGL) or MP DSDs retrieved from MRR Z (at 2250 m AGL) respectively when compared to rain gauge records. By varying the height of the model rainshaft over time to reflect transient shifts in bright-band level (Fig. 2), the difference between modeled surface rainrate and rain gauge records is reduced to −45% using MRR DSDs at variable heights (2250 m/2400 m AGL) as top boundary condition (Fig. 10a and b). The MRR DSD (Fig. 11a) is characterized by a larger number of small (d < 0.25 mm) and large (d > 3 mm) drops, but a smaller number of mid-size (0.75 mm < d < 2 mm) drops when compared to the MP DSD (Fig 11b). However, in both cases, a bias is likely to be introduced by the calibration uncertainties mentioned previously and MRR-RG-Model comparison are consistent with the underestimation of the rainrate and total accumulated water observed for MRR1 (Fig. 4a and c).

For the fall event (Fig. 10b and d: Table 2 – Event #9), important differences are found when using one or the other boundary condition with a difference model/RG of +100% when using MRR DSDs, and about −35% when using MP48 DSDs from reflectivity Z (Fig. 10d). The MRR DSD algorithm grossly overestimates the rainrate suggesting that the true DSD distribution in the fall is very different than that shown in Fig. 9b. Both DSDs (MRR DSDs: Fig 11c; MP DSD from Z: Fig. 11d) are comparable for large drop sizes (d > 1 mm), while for the MRR DSDs, the concentration of small raindrops (d < 1 mm) is 100 fold higher than the classical value (No = 0.08 cm^{-4}) used in the Marshall–Palmer distribution (Marshall and Palmer, 1948; Prat and Barros, 2009). The very high proportion of small drops could lead to enhanced coalescence effects resulting into an overestimation of surface rainrates by the model. There is a large uncertainty regarding the amount of small drops in the DSD that cannot be investigated with the current objects at our disposal (Barros et al., 2008). However, the region of the Great Smoky Mountains is characterized by widespread pres-

ence of fog, drizzle, and low level clouds (thus "smoky"), and a large population of small drops (d < 0.5 mm) is not unexpected. A simple numerical experiment for the summer case 07/29/08 using a Marshall–Palmer distribution with an increased proportion of small drops (No = 0.8 cm^{-4} and up to No = 4 cm^{-4}) suggests significant improvements in the surface rainrate associated with enhanced coalescence processes as compared to observations (not shown). It is therefore critical that attention be paid to the description of the left-hand side of the DSD in future observational campaigns. Nonetheless, another source of uncertainty could also be introduced by the presence of ice particles even if boundary conditions (h = 1050 m) were selected below the bright-band (∼1300 m) based on the vertical profiles of reflectivity (Z) for this rain event (not shown). Finally, regardless of the boundary conditions used (MRR DSD or MP DSD), the model is able to simulate the dynamics of the rain event when compared to the rain gauge records and to improve the timing of the surface rainrate MRR estimates.

This modeling experiment illustrates well the challenges with radar retrieval generally and the need for more physically-based algorithms in radar applications, especially for science oriented studies. This is critical for light rainfall given the widely acknowledged ambiguity in the Z–R relationships (Matrosov, 2005; Rose and Chandrasekar, 2007). Furthermore, this experiment emphasizes the importance of a better description of drop distributions in the lower end of the spectra (d < 0.3 mm), a domain where most sensors are not operational or have limited sensitivity (Barros et al., 2008).

6. Summary and conclusion

In this paper, MicroRain radar observations from two field campaigns in the GSMNP are presented. Conditions such as warm (summertime) and cold (fall) precipitation are compared as well

as mountain vs. valley precipitation. Collocated rain gauge data are compared with MRR records. The main conclusions for this study can be summarized as follows.

6.1. Summer vs. fall precipitation at the mountain ridge

The daily rain gauge records of summertime precipitation are step shaped with about twice as long duration after 9:00EST (15%) than before (7%), while fall records for rainfall present a double peaked curve with maxima above 20% for early morning (6:00–9:00) and late afternoon (15:00–18:00). In both cases, about 60% of the accumulated rainwater comes from afternoon precipitation (12:00–21:00). In addition, summertime precipitation presents higher rain rates with average values above 4 mm h^{-1} and above 10 mm h^{-1} in case of late afternoon precipitation (15:00–18:00) corresponding to mountain thunderstorms. By contrast, fall precipitation is characterized by an almost constant rain rate throughout the day (1.5–4 mm h^{-1}). Moreover, relying on rain gauge records for the distinction between convective (>10 mm h^{-1}) and stratiform (<10 mm h^{-1}) events, the data show that although convective events account for only 4% in terms of rainfall duration, they provide about 40% of the precipitated water at the mountain ridge during summertime. Finally, compared to fall rainfall, summertime precipitation at higher elevation is characterized by heavier right tail DSD spectra that support the hypothesis of enhanced coalescence microphysics due to orographic effects.

6.2. Ridge vs. valley precipitation

MRR deployments in the fall at both locations showed that for the same period precipitation (snow/rain) occurred about three times more often at the mountain ridge than in a valley adjacent at a location about 15 km away. The difference in the total rain accumulation was found to be on the order of 100% at the ridge site. For concurrent rain events, the difference in rainfall measured is 60% higher at the mountain ridge than in the valley. Analysis of the diurnal cycle for precipitation, indicated that nighttime events at higher altitude were mostly snow events, while MRR records for rainfall only indicated a large number of events with low-moderate intensity for the early morning (6:00–9:00) and a decrease in number/increase in intensity for the afternoon (15:00–18:00). At lower elevation, precipitation was mostly rain with a large number (40%) of early morning events (6:00–9:00). In addition, rainfall at higher elevations is characterized by higher rain intensity with a maximum of 5.3 mm h^{-1} observed in the afternoon (15:00–18:00) compared to 2.6 mm h^{-1} observed early morning (6:00–9:00) at lower elevations. From a microphysical perspective, no noticeable differences were observed between drop spectra at both elevations during the fall deployment, consistent with predominantly stratiform rainfall.

6.3. MRR estimates vs. rain gauge records

Comparisons of collocated rain gauges and MRR records show that both sensors provided similar qualitative description for the precipitation events in term of duration and dynamics. In addition, MRR were found particularly useful in case of cold precipitation, as they are able to provide an accurate picture of the transition from rain to snow while rain gauges and weather transmitter systematically missed snow events as they occurred and only recorded delayed tips due to snow melt (rain gauge only). However, when taking the rain gauge as the reference for the measurement of the surface rain rate, the MRR was found to underestimate or overestimate the quantity of water accumulated by as little as 600% and as high as 200% respectively. Therefore, a reliable quantitative estimate of rainfall and intensity depends on the determination of calibration constants that will allow an adjustment of MRR records afterwards. As shown in this work, on-site calibration has to be performed for the adjustment of rainfall measured by the MRR.

6.4. MRR microphysical properties

Evidence of a seasonal signature was found with significantly heavier tails for summer DSDs at higher elevations due to orographic enhancements effects, while no significant differences were observed between ridge and valley locations during fall deployment. This study suggests that further research is needed to characterize the DSD in the range of very small diameters ($d < 0.5$ mm), and/or as it concerns the ability to separate rainfall events to snow/ice or mixed rain events.

More importantly, in order to achieve a reliable physically based retrieval of rain rate at ground levels using a microphysical model (Prat and Barros, 2007a,b), reliable measurements of the storm properties are needed at a given altitude of the atmosphere (Prat et al., 2008; Prat and Barros, 2009). This work showed that the MRR can be useful in drawing a reliable qualitative picture of the evolution of storms at local places and to distinguish rain from snow events in the inner regions of mountain systems. However, from a quantitative perspective, significant differences were observed when compared with other sensors such as rain gauges with over/underestimation of rain rate and cumulative rainfalls. Further numerical experiments using a microphysical model (Prat and Barros, 2007a,b) emphasized those uncertainties as it concerns the MRR "built-in" internal rainfall estimation algorithm. Finally, the comparison of the MRR and rain gauges data and the use of both collocated devices allowed us, in the case of cold precipitation, to distinguish rain and melting snow accumulated in the funnel which would have been otherwise impossible to separate from the rain gauge record only. In order to capture the whole precipitation cycle without ambiguity, we suggest the use of low cost radiofrequency snow pack sensors (Kang and Barros, accepted for publication) that are currently being developed and from whom the first laboratory and in situ tests have been found promising.

The two main causes of uncertainty in MRR QPE come from (1) calibration issues and agreement between radar data and ground sensors (Löffler-Mang et al., 1999; Peters et al., 2002), and (2) the difficulty to separate snow/drizzle/rain transition unambiguously (Cha et al., 2009). In this work, the MRR was found complementary to rain gauge records and particularly useful to (1) identify the type of precipitation and thus provide a distinction between snow melt and precipitation (even if a separation a priori of rain/drizzle/snow records is particularly challenging) and (2) detect light rainfall (>0.01 mm h^{-1}) as compared to rain gauges ($\approx$0.1 mm h^{-1} or higher). Because of their mobility and modest cost, MRRs offer one interesting opportunity to improve the monitoring of the 3D structure of precipitation in regions of complex terrain, though caution must be exercised with regard to data analysis and interpretation. This work represents the first analysis of several planned field campaigns aimed at understanding the mechanisms of orographic precipitation in the inner regions of mountain systems. Observations from similar deployments are planned to be multiplied in a near future, with the goal of evaluating the fidelity of existing cloud-resolving models and to test new parameterizations for the representation of boundary-layer and rainfall processes in mountainous regions.

References

Atlas, D., Srivastava, R.C., Sekhon, R.S., 1973. Doppler Radar characteristics of precipitation at vertical incidence. Rev. Geophys. 11 (1), 1–35.

Barros, A.P., Kuligowski, R.J., 1998. Orographic effects during a severe wintertime rainstorm in the Appalachian Mountains. Mon. Weather Rev. 126, 2648–2672.

Barros, A.P., Lettenmaier, D.P., 1993. Dynamic modeling of the spatial-distribution of precipitation in remote mountainous areas. Mon. Weather Rev. 121 (4), 1193–1214.

Barros, A.P., Lettenmaier, D.P., 1994. Dynamic modeling of orographic induced precipitation. Rev. Geophys. 32 (3), 265–284.

Barros, A.P., Tao, K., 2008. A space-filling algorithm to extrapolate narrow-swath instantaneous TRMM microwave rain-rate estimates using thermal IR imagery. J. Atmos. Oceanic Technol. 25 (11), 1901–1920.

Barros, A.P., Joshi, M., Putkonen, J., Burbank, D.W., 2000. A study of the 1999 monsoon rainfall in a mountainous region in central Nepal using TRMM products and rain gauge observations. Geophys. Res. Lett. 27 (22), 3683–3686.

Barros, A.P., Prat, O.P., Shrestha, P., Testik, F.Y., Bliven, L.F., 2008. Revisiting low and list (1982): evaluation of raindrop collision parameterizations using laboratory observations and modeling. J. Atmos. Sci. 65 (9), 2983–2993.

Cha, J.W., Chang, K.H., Yum, S.S., Choi, Y.J., 2009. Comparison of the bright band characteristics measured by micro rain radar (MRR) at a mountain and a coastal site in South Korea. Adv. Atmos. Sci. 26, 211–221.

Ciach, G.J., 2003. Local random errors in tipping bucket rain gauges measurements. J. Atmos. Oceanic Technol. 20, 752–759.

Ciach, G.J., Krajewski, W.F., 1999. Radar-rain gauge comparisons under observational uncertainties. J. Appl. Meteor. 38, 1519–1525.

Foote, G.B., DuToit, P.S., 1969. Terminal velocity of raindrops aloft. J. Appl. Meteor. 8, 249–253.

Habib, E., Krajewski, W.F., Kruger, A., 2001. Sampling errors of tipping-bucket rain gauge measurements. J. Hydrol. Eng. 6, 159–166.

Kang, D.K., Barros, A.P., accepted for publication. Introducing an L-band Snow sensor system for in situ monitoring of changes in water content: system testing under laboratory and field conditions. IEEE Trans. Geosci. Remote Sens.

Lang, J.L., Barros, A.P., 2002. An investigation of the onsets of the 1999 and 2000 monsoons in central Nepal. Mon. Weather Rev. 130, 1299–1316.

Lang, J.L., Barros, A.P., 2004. Winter storms in the central Himalayas. J. Meteor. Soc. Jpn. 82 (3), 829–844.

Löffler-Mang, M., Kunz, M., Schmid, W., 1999. On the performance of a low-cost K-Band Doppler radar for quantitative rain measurements. J. Atmos. Oceanic Technol. 16, 379–387.

Marshall, J.S., Palmer, W.McK., 1948. The distribution of raindrops with size. J. Meteor. 5, 165–166.

Matrosov, S.Y., 2005. Attenuation-based estimates of rainfall rates aloft with vertically pointing Ka-band radars. J. Atmos. Oceanic Technol. 22, 43–54.

Metek, 2009. MRR Physical Basics. Version 5.2.0.1, 20pp.

Miller, D., Wilson, A., Cutrell, G., Barros, A.P., Prat, O.P., submitted for publication. Observed precipitation associated with air mass thunderstorms over the Southern Appalachian Mountains 28, 29 July 2008. Nat. Hazards Earth Syst. Sci.

Perry, L.B., Konrad, C.E., 2006. Relationships between NW flow snowfall and topography in the Southern Appalachian, USA. Climate Res. 32, 35–47.

Peters, G., Fischer, B., Andersson, T., 2002. Rain observations with a vertically looking Micro Rain Radar (MRR). Boreal Environ. Res. 7, 353–362.

Peters, G., Fischer, B., Münster, H., Clemens, M., Wagner, A., 2005. Profiles of raindrop size distributions as retrieved by microrain radars. J. Appl. Meteor. 44, 1930–1949.

Prat, O.P., Barros, A.P., 2007a. A robust numerical solution of the stochastic collection-breakup equation for warm rain. J. Appl. Meteor. Climatol. 46 (9), 1480–1497 (PB07a).

Prat, O.P., Barros, A.P., 2007b. Exploring the use of a column model for the characterization of microphysical processes in warm rain: results from a homogeneous rainshaft model. Adv. Geosci. 10, 145–152 (PB07b).

Prat, O.P., Barros, A.P., 2009. Exploring the transient behavior of Z–R relationships: implications for radar rainfall estimation. J. Appl. Meteor. Climatol. 48 (10), 2127–2143 (PB09).

Prat, O.P., Barros, A.P., Williams, C.R., 2008. An intercomparison of model simulations and VPR estimates of the vertical structure of warm stratiform rainfall during TWP-ICE. J. Appl. Meteor. Climatol. 47 (11), 2797–2815 (PBW08).

Roe, G.H., 2005. Orographic precipitation. Annu. Rev. Earth Planet. Sci. 33, 645–671. doi:10.1146/annurev.earth.33.092203.122541.

Rose, C.R., Chandrasekar, V., 2007. Systems engineering analysis of a TRMM PR-like rainfall retrieval algorithm. IEEE Trans. Geosci. Remote Sens. 45 (2), 426–434.

Sieck, L.C., Burges, S.J., Steiner, M., 2007. Challenges in obtaining reliable measurements of point rainfall. Water Resour. Res. 43, W01420. doi:10.1029/2005WR004519.

Smith, R.B., 1979. The influence of mountains on the atmosphere. Adv. Geophys. 21, 87–233 (Academic Press).

Smith, R.B., Jiang, Q., Fearin, M.G., Tabary, P., Dorninger, M., Doyle, J.D., Benoit, R., 2003. Orographic precipitation and air mass transformation: an Alpine example. Quart. J. Roy. Meteor. Soc. 129, 433–454. doi:10.1256/qj.01.212.

Smith, R.B., Barstad, I., Bonneau, L., 2005. Orographic precipitation and Oregon's climate transition. J. Atmos. Sci. 62, 177–191.

Wang, J., Fisher, B.L., Wolff, D.B., 2008. Estimating rain rates from tipping bucket rain gauge measurements. J. Atmos. Oceanic Technol. 25, 43–56.

Wooten, R.M., Gillon, K.A., Witt, A.C., Latham, R.S., Douglas, T.J., Bauer, J.B., Fuemmeler, S.J., Lee, L.G., 2008. Geologic, geomorphologic, and meteorological aspects of debris flows triggered by Hurricanes Frances and Ivan during September 2004 in the Southern Appalachian Mountains of Macon County, North Carolina (Southeastern USA). Landslides 5 (1), 31–44.